PAPER • OPEN ACCESS

A continuously scanning separate-crystal single-photon x-ray interferometer

To cite this article: B Andreas and U Kuetgens 2020 *Meas. Sci. Technol.* **31** 115005

View the article online for updates and enhancements.

A continuously scanning separate-crystal single-photon x-ray interferometer

B Andreas and U Kuetgens

PTB—Physikalisch-Technische Bundesanstalt, Bundesallee 100, 38116 Braunschweig, Germany

E-mail: birk.andreas@ptb.de

CrossMark

Abstract
The feasibility of a new design and measurement concept of a combined optical and x-ray interferometer (COXI) is demonstrated here. Mechanical noise in the x-ray interferometer can be cancelled efficiently with fast and synchronous detection of the optical interferometer phase and x-ray counts. The scan-length requirement of the decadic step method of conventional COXI setups is reduced by more than one order of magnitude due to the correlation between single-photon interference events. The actual scan length of the shown setup is limited to 4 μm. It is estimated that a future update will enable us to measure the lattice parameter of ^{28}Si, at least with the targeted relative statistical reproducibility of 3×10^{-9}.

Keywords: fundamental constants, metrology, interferometers, x-ray interferometers, length measurement

(Some figures may appear in colour only in the online journal)

1. Introduction

The first x-ray interferometer (XRI) was demonstrated by Bonse and Hart in 1965 [1]. Before their setup is described, a brief introduction to the features relevant to x-ray interferometry are given without going too much into the details of the by now well-established dynamical diffraction theory [2–4]. It is this theory which is essential for the understanding of the following content.

If an electromagnetic wave is incident at a periodic structure whose period d is similar to the wavelength λ, then a diffracted wave is formed. For sake of simplicity let us assume a plane wave incident at an infinitely extended sinusoidal grid. The situation is best described in reciprocal space:

$$\mathbf{k}_h = \mathbf{k}_0 + \mathbf{h}, \tag{1}$$

where $\mathbf{k}_0$ is the wave vector of the incident, $\mathbf{k}_h$ the one of the diffracted wave and $\mathbf{h}$ is the grid vector. The vector lengths are defined by $|\mathbf{k}_0| = 2\pi/\lambda$ and $|\mathbf{h}| = 2\pi/d$. The math gets more involved when the grid becomes an extended 3D structure—e.g. the atomic lattice of a crystal. Equation (1) basically states that momentum is conserved. This is sufficient to describe very thin grids. However, energy is also a conserved quantity, and as soon as thick crystals are at play, the energy which is contained in the diffracted wave is missed in the other—i.e. transmitted—wave. Furthermore, from the diffracted wave a part can be diffracted back into the original direction and so forth. Together with the boundary conditions at the crystal's interfaces, the complex susceptibilities χ_0 and χ_h[1], and Maxwell's equations, this complicated interplay can be described and the propagating modes in the crystal as well as the electromagnetic field at the interfaces can be found [2–4]. For extended dynamical diffraction theory four solutions are considered

---

[1] These quantities have to be calculated for every treated orientation of the considered crystal from knowledge about its unit cell and the atomic scattering factors at the relevant radiation energy [5, 6].

owing to the possibility to have for both—i.e. transmitted and diffracted wave—forward and backward direction [2].

If the crystal is only weakly absorbing the found solutions are very sensitive to the conditions at both interfaces and their distance—i.e. the thickness of the crystal. One can interpret this as reflection on the inside of the interfaces with several round-trips. The exiting waves contain contributions of different orders of round-trips and can interfere in intricate ways, depending on miniscule phase effects. We should quickly note here that one commonly refers to two different geometries depending on the side of the crystal on which the diffracted wave exits with respect to the incoming wave. One of them is the *Bragg geometry*. Here, we solely consider the *Laue geometry*, i.e. the diffracted (and also the transmitted) wave exit on the opposite side from where the incoming wave enters. If the crystal is strongly absorbing, only the zero-order forward-propagating modes deliver a significant contribution to the exiting waves. The relevant differences between the weak and the strong regime are further investigated in section 2.4.

Dynamical diffraction theory also correctly describes anomalous transmission and absorption—i.e. the *Borrmann effect* [7]. It can be interpreted as follows: under the right conditions the transmitted wave field can have the knots or crests at the atom positions which results in extraordinary high transmission or absorption, respectively.

Another effect is the *Borrmann fan* [7]. Due to the above-mentioned dynamic interplay between transmitted and diffracted wave the wave field spreads on its way through the crystal which results in a broadening of the width of the exiting beams proportional to the thickness and inversely proportional to the Bragg angle.

A sketch of the Bonse and Hart XRI is depicted in figure 1. It consists of a monolithic single-crystal silicon block with three equally thick and evenly spaced lamellae on top of it. The (220)-reflection of Cu-K$_\alpha$ radiation is transmitted anomalously, i.e. by Borrmann effect [7], in Laue geometry. The lamellae serve in sequence as the beam splitter, mirror, and analyzer. The main principle of this arrangement is the moiré effect between the waves formed by splitter and mirrors in the analyzer and the crystal lattice of the analyzer. It is well worth emphasizing that the periodicity of the resulting moiré does not depend on the x-ray wavelength but on the crystal lattice [1]. It is also worth mentioning that some geometrical design restrictions are mandatory to actually achieve interference. For the *focusing condition*—i.e the condition that the two beam paths meet just at the correct distance to cross in the analyzer—it is necessary to have equally thick splitter and mirror lamellae. Secondly, the sum of both gap widths has to be equal between both paths. This also ensures that spatial [8] and temporal² coherence can be realized with crystallographic x-ray tubes. Furthermore, the crystal lattice has to be oriented almost identical in all lamellae. Bonse and Hart achieved this by the monolithic design.
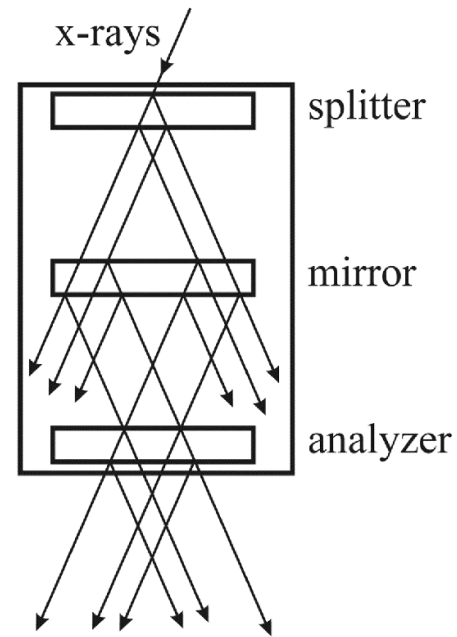
Figure 1. Simplified sketch of the Bonse and Hart XRI [1]. The dimensions are not to scale. Particularly, the lamellae are depicted extraordinary thick to better visualize the beam broadening by the Borrmann fan phenomenon [7].

Also in 1965, Lang pointed out that it should be possible to relate the lattice spacing of a moving crystal with the wavelength of an optical interferometer by counting the respective fringes [9]. For this however, the static design cannot be used because the analyzer cannot be moved with respect to the wave field.

After the first static demonstrator, the triple Laue-case (LLL) interferometer evolved. In 1968, Hart was the first who translated the analyzer by using a monolithic hinge design which ensures that the lattice planes of the analyzer crystal remain inside the acceptable angular range [10]. However, owing to mechanical stress constraints, such monolithic designs cannot surpass a certain travel range [11]. In the same year, Bonse and te Kaat [12] demonstrated a design with separate analyzer crystal which provided full angular control by using three x-ray sources and additional diffraction channels. However, no translation mechanism had been included. Then, in 1969, Deslattes reported also a separated analyzer on top of a monolithic brass hinge structure [13]. This setup was also the first where an optical interferometer could measure the displacement of the analyzer. A stroke of at least 20 μm was possible. Shortly afterward, Bonse *et al* demonstrated the 300 μm travel range by using a leaf spring mechanism claiming improvability up to 600 μm [14]. They used an optical Fabry-Pérot interferometer to observe the translation and could measure in vacuum. In 1974, Becker and Bonse introduced a skew-symmetric two-crystal design for angle measurements which is insensitive to translation [15].

The working principle of the combined optical and x-ray interferometer (COXI) is demonstrated in figure 2 with a

---

² Characteristic x-rays emitted by a crystallographic x-ray tube have typical coherence lengths of less than a micron. However, the narrow angular acceptance of the XRI increases this to several microns.
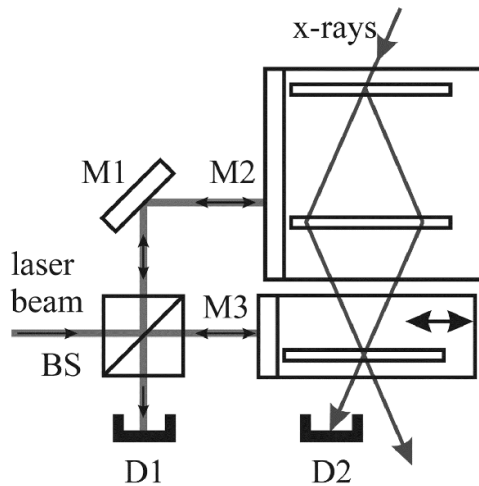
Figure 2. Schematic of a combined optical and x-ray interferometer (COXI). A Michelson-type optical interferometer consisting of the beam splitter BS, mirror M1, reference mirror M2, and moving mirror M3 measures displacements of the separated analyzer lamella of the LLL XRI (cf. figure 1) in D1. The moiré fringes of the XRI are detected in D2.

Michelson-type optical interferometer consisting of the beam splitter BS, mirror M1, reference mirror M2, and measurement mirror M3. The separate analyzer crystal can be translated in the indicated direction. Moiré fringes in D2 are simultaneously detected with the optical fringes in D1. This allows the direct comparison of the crystal's lattice spacing to the wavelength of the laser [13].

In order to avoid detrimental influences on the optical phase the preferred medium for such a kind of setup should be vacuum. Otherwise, for instance in air, fluctuations, temperature gradients, humidity, and insufficient knowledge on the refractive index of the immersion medium limit the accuracy of the comparison. Therefore, such a setup, just like the setup shown later, must reside in a vacuum chamber. The optical interferometer must not necessarily be of Michelson type. It is chosen in figure 2 for the sake of simplicity.

Soon after the invention of the LLL XRI, the possibility to accurately measure the lattice parameter of silicon was exploited for the so-called x-ray crystal density (XRCD) method where it is a central feature until today [16–27]. The XRCD method can be described as follows: by knowing the lattice parameter and isotopic composition of a macroscopic single crystal, it is possible to relate the microscopic volume and molar mass of its unit cell to the macroscopic volume and mass. Before the last revision of the SI, this 'atom counting' was used to measure Avogadro's number N_A. The XRCD method played an important role in the re-definition of the kilogram based on the Planck constant h, which can be related to N_A via the molar Planck constant $N_A h$ [22–26]. Now, after the revision of the SI in 2019, N_A and h are fixed values and enable the realization of the kilogram also by XRCD [27].

Before the International Avogadro Coordination (IAC) was founded to re-define the kilogram by accurately measuring N_A, four national metrology institutes had completed absolute lattice parameter measurements: IMGC (later: INRIM), NIST,

NMIJ, and PTB [18]. However, as the project evolved, only IMGC/INRIM maintained its capability. Thus, the measurements of central importance—i.e. the measurements of the ^{28}Si lattice parameter of the IAC crystal—have been measured only by INRIM [20, 21]. Therefore, the need to have at least one other independent measurement arose, leading to the efforts to realize an XRI at PTB with a relative statistical reproducibility for d_{220} of 3×10^{-9}. The scanning mechanism of the INRIM apparatus and the measurement principle are described in [28]. This setup is limited mainly by drift and the x-ray photon count rate which enables at most a scanning speed of 1 nm/s. Therefore, a continuous measurement over its maximal travel range of 5 cm is not feasible, and only short range measurements at locations separated by distances increasing in the decadic logarithmic scale are done. Thus, at each step, the accuracy of the predicted number of lattice planes increases by one order of magnitude. For instance, segments of approx. 1 mm length had to be measured to yield a relative uncertainty of 1.75 nm/m [21].

In 1999, Rode and Jex used a monolithic symmetric LLL silicon XRI with an acoustically excited and split mirror lamella to demonstrate heterodyne quantum beating of Cu-K$_\alpha$ x-ray photons [29]. This laid the basis to the main idea of how to increase the scanning speed of an XRI: to recognize that, above background, every registered photon is a single-photon, self-interference event. This means that almost all events counted during a scan are correlated via the moving crystal lattice. A Fourier transform of the time series of a counting channel should reveal the crystal's periodicity at a certain fringe frequency, depending on the chosen scan speed, even if the sampled data appears to be completely noisy [30].

In this paper, we will demonstrate by experimental results how this idea enables a faster scanning speed, while simultaneously the scan-length requirement of the above-described decadic stepping method can be reduced by more than one order of magnitude. We also present a new interferometer design and measurement concept, which enables continuous scanning over the full travel range while maintaining angular control at the sub-nanoradian level. This is especially important because it helps to minimize the well-known Abbe error— i.e. the error $\Delta l = r \sin\beta$, where β is a guiding error angle of an axis shifted by the offset length r from the axis from which the length data is actually obtained. Together with temperature, the Abbe error is often the dominating effect in length measurements [31].

In the next section, the measurement setup and procedure are presented. Then, we show current results based on 4 μm scans, discuss them, look into the near future, and conclude.

2. Methods

2.1. Main concept

In figure 3(a), the skew-symmetric layout of our COXI is sketched. The description of the optical part is given in section 2.3. The unique feature of the shown design is the integration of two XRI into one setting. The red paths (dark gray in printed version) are used in the interferometer sensitive to

translation l—this is actually the COXI part—while the yellow paths (thick light gray) branch off from the red paths to complete the interferometer sensitive to angle θ. The angle interferometer resembles the skew symmetric two-crystal interferometer [15], except for one additional transmission in each path. Since every transmission reduces the photon flux roughly by one order of magnitude, this can be seen as a disadvantage that, however, is not too detrimental in our case. This configuration is insensitive to translation and primarily detects changes in θ [32].

The XRI consists of two separated monolithic parts—i.e. the upper splitter/mirror crystal and the lower analyzer crystal—with thin lamellae (thickness $\lesssim 0.5$ mm, height $= 10$ mm) on top of a 15 mm high base (cf. figure 4). The laser beams in green (thin light gray) are reflected by the flat polished left sides. The analyzer crystal is mounted on the stage depicted in figure 3(b). The stage consists of an aluminum flexure hinge glued on two piezoelectric shear actuators (red / dark gray) of type PICA P-143.03 from Physik Instrumente [3]. Their dimensions in x-, y-, and z-direction are: 10 mm, 10 mm, and 15.5 mm, respectively. These actuators allow elevation in the z- and shearing in the x- and y-direction. The nominal travel range at a supply voltage between -250 V and 250 V is 3 µm $\pm$ 0.9 µm along each dimension. The relevant degrees of freedom and their dependence from the actuation effect are indicated by double arrows and appear also in the coordinate system of figure 3(a), where θ and ρ adhere to the direction of their respective rotation axes.

2.2. Si crystal

The crystal parts, depicted in figure 4, are made from the first single crystal that had been float-zone grown from isotopically enriched, high purity, and undoped ^{28}Si by the Leibniz-Institut für Kristallzüchtung in Berlin inside the framework of the IAC [22, 23]. The two crystal parts were machined as follows: first, the raw form was cut out from the silicon boule by a diamond wire saw. Then the orientation of the crystal's side face with respect to the (220)-lattice planes was refined by crystallographically oriented cutting within a few arcsec by a diamond saw. These kind of crystal orientation is a standard procedure with the PTB's crystal orientation apparatus [4]. Afterwards, the side faces—i.e. the later side mirrors—were polished to optical quality ($\lambda/20$). Then the lamellae were carved out by a high-precision rotating diamond tool which was driven by a high-speed air turbine [33]. Finally, the machining was completed by separating the two parts by a diamond saw. The last

step of the manufacturing process was to protect the optical mirrors with adhesive foil and wet isotropic etching the bodies with a mixture of HNO_3, HF, and $H_3C\text{-}COOH$ [34] by about 50 µm on each side in order to remove the residual mechanical stress induced by the machining. A last check with the orientation apparatus revealed that the targeted orientation could be reached with tolerable deviations of 4 arcsec in θ and 7 arcsec in ρ.

2.3. Optical interferometers

The optical part of the COXI actually consists of two heterodyne interferometers which are fed via polarization-maintaining fibers [35]. Basically, it is the vacuum version of a very similar setup which was introduced earlier and has been operated in air [36]. The actual interferometer setup is sketched in figure 5. Two frequencies $f_r = f_L + 76.25$ MHz and $f_m = f_L + 80$ MHz, where $f_L = 563,212,634,599.7$ kHz is the laser frequency, are used for both interferometers which we refer to as reference and measurement interferometer. The frequencies $f_{r,m}$ are obtained from the respective $+1$st order of two acousto-optical modulators (AOM) and then coupled into the respective fibers which are fed through the vacuum chamber into the interferometer setup. The laser source, a frequency-doubled Nd:YAG laser [36, 37], the AOM, and the fiber-coupling are on a separate optical table in a different room. It is worth noting that the first beam splitting appears on this table. Therefore, the paths through AOM, coupling, and fibers would normally contribute to the interference. However, it is shown below how the respective contributions are cancelled in the presented setup.

The light of both fibers is collimated, sent through Glan-Thompson polarizers, split by a non-polarizing beam splitter plate (BS), and reflected at a polarizing beam splitter plate (PBS). Thus, four beams are generated which are labeled Mm, Mr, Rm and Rr, where the capital letters denote the interferometer and the lowercase letter indicate the frequency, e.g. Mr means reference beam of the measurement interferometer. All four beams are passing through individual quarter-wave plates (QW) which turn the linearly polarized beams into circularly polarized ones. After reflection at the polished sides of the XRI crystals, the second passage through the QW makes the light linearly polarized again. However, it is now orthogonally polarized to the former state and hence is now transmitted through the PBS. The step mirror (SM) reflects the beams in a way that allows the combination of the beams Mm with Mr to Mmr and Rm with Rr to Rmr at the second BS. The combined beams are directed via SM through respective Glan polarizers (GP), QW, and focused by lenses (L) to the respective detectors $D_{R,M}$. The combination of GP and QW blocks light that is reflected at the L and $D_{R,M}$.

The heterodyne signals with frequency $f_H = f_m - f_r$ measured by $D_{R,M}$ are formed by the beating between the respective measurement and reference beams. The signals are then amplified just outside the vacuum chamber and transmitted to analog-to-digital converters and evaluated on a field-programmable gate array (FPGA). For the sake of brevity, the

---

[3] This is not a recommendation. We include these details for better replicability.

[4] The main principle is the necessary invariance of the symmetric Bragg condition under rotation of the crystal sample. When the lattice planes are oriented—i.e. the lattice plane normal coincides with the rotation axis—the tumbling of the surface, observed by an auto-collimator, reveals its orientation with respect to the crystal lattice. A reference mirror which is mounted on the sample holder is adjusted parallel to the sought lattice planes. This reference mirror is then used to orient the sample to a machining tool's reference mirror.
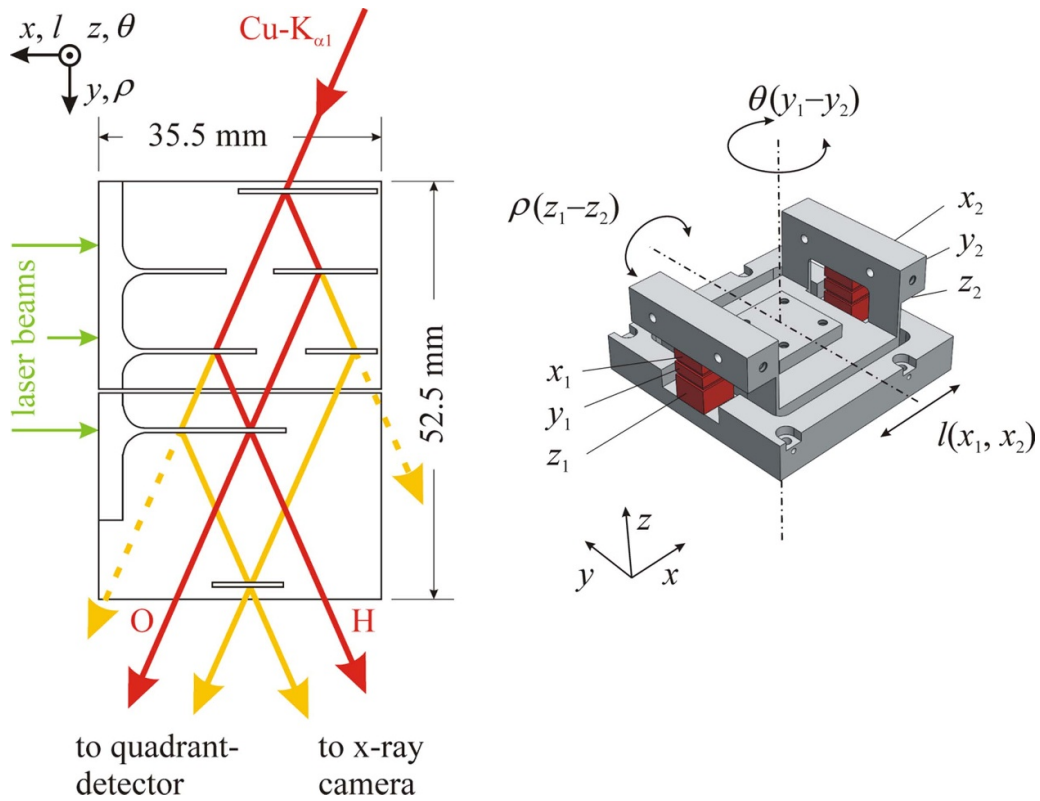
Figure 3. (a) Sketch of a combined XRI for translation (red paths) and angle (yellow paths). The dashed paths are not used. The laser beams (green) belong to two optical interferometers which are sketched in detail in figure 5. The letters O and H denote the output O- and H-beam [1]. (b) Flexure hinge stage to control translation l along x and rotation by angles θ around z and ρ around y by the use of piezoelectric shear actuators (red) providing the indicated degrees of freedom. The colors only appear in the online version.
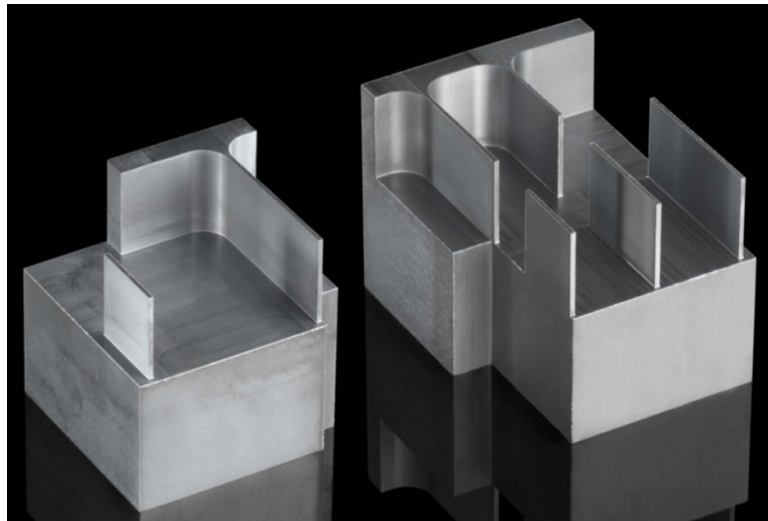

Figure 4. Crystal parts of XRI sketched in figure 3(a) made of the ^{28}Si-enriched IAC crystal [22, 23] before etching.

details of the optical-phase evaluation will be communicated in a forthcoming paper. Here, the important information is that the respective phases of the reference and the measurement interferometer $\phi_{R,M}$ are subtracted:

$$\phi = \phi_M - \phi_R, \tag{2}$$

where ϕ is the optical phase used further. This means that all parasitic effects—e.g. thermo- or elasto-optic disturbances in the fibers—that shift the phase in the reference and the measurement light but also common motion between XRI and the rest of the setup are detected in both interferometers identically and therefore cancel out. Only the phase shift induced by the analyzer crystal translation into the beam Mm survives this differential referencing.
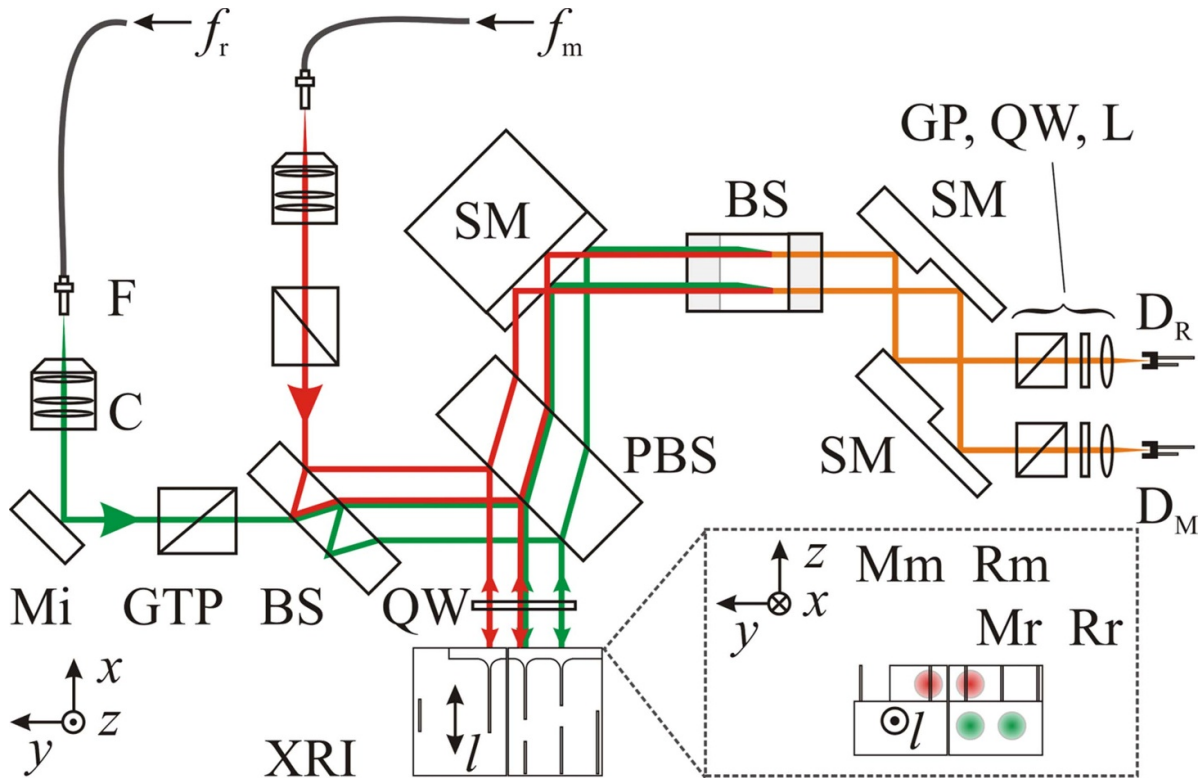
Figure 5. Sketch of the two optical heterodyne interferometers with reference and measurement frequencies f_r and f_m. The reference and measurement beams are in green and red, respectively (the colors appear only in the online version). The slight shift between the red and green paths indicate that they are arranged vertically as indicated in the inset. The arranged letters in the inset correspond to this arrangement of the beams and represent also the used labels: M and R refer to measurement and reference interferometer while m and r refer to measurement and reference beam or frequency, respectively. The orange paths indicate where the beams are combined—i.e. collinear. It is F: fiber ferrule, C: collimator, Mi: mirror, GTP: Glan-Thompson polarizer, BS: non-polarizing beam-splitter plate, PBS: polarizing beam-splitter plate, QW: quarter-wave plate, XRI: the x-ray interferometer depicted in figure 3(a), SM: step mirror, GP: Glan polarizer, L: focusing lens, $D_{R,M}$: detectors of reference and measurement interferometer.

2.4. X-radiation

The x-rays are produced in the line-focus of a crystallographic tube with the Cu target at 40 kV with a current of 30 mA. We chose Cu-K$_\alpha$ radiation to operate in the strong-absorption regime. This has many advantages. First of all, the contrast is less dependent on the manufacturing tolerances [8, 38, 39]. To illustrate the strong- and weak-absorption regimes, figure 6 compares for 0.4 mm thick lamellae fringe visibility and phase over the analyzer thickness variation and displacement along y for O- and H-beam (cf. figure 3(a)) of Cu-K$_\alpha$ and Mo-K$_\alpha$ radiation, respectively. With Cu-K$_\alpha$, the variations are much less perturbing as with Mo-K$_\alpha$. To obtain the same insensitivity with Mo-K$_\alpha$, the lamellae had to be approx. 4 mm thick in order to operate in the strong absorption regime. This would increase the Borrmann fan, and hence the width of the beams, roughly by one order of magnitude. Also, the Bragg angle would be smaller. In summary, a less compact setup with larger crystal parts is required to separate the beams. More from the scarce and expensive ^{28}Si material is needed, and self-weigh deformation plays a significant role [40]. Additionally, it is far more easy to manufacture satisfactory mirror optics for the collimation of Cu-K$_\alpha$ than for Mo-K$_\alpha$ radiation.

In our setup, a curved multilayer monochromator diffracts Cu-K$_{\alpha 1}$ radiation parallelly collimated toward the experiment. The resulting 1 mm wide and vertically diverging x-ray beam enters through a 25 μm thick polyimide-foil window into the evacuated chamber, which provides a residual pressure of approx. 30 mPa, and traverses a brass mask (height: 8 mm, width: 6 mm), just before the entry position of the interferometer at a distance of approx. 80 cm from the x-ray source. The width of 6 mm is adapted to the useful corridor. The aperture of the mask is elevated by 1 mm above the lamellae feet and hence the beams do not reach to the lower and upper edges of the lamellae. It is worth noting that the vertical extension enables the retrieval of information about the ρ-angle, as we will show below. The beams leave the chamber again through two respective vacuum windows before detection. The beams going to the right are directed toward an x-ray camera comprising the scintillator, intensifier, and CCD. The beams traveling to the left are measured by a quadrant photomultiplier scintillation detector in such a way that one obtains two vertical channels respectively. The ones for the θ-angle have no additional purpose, while both COXI channels inherit important information also on the ρ-angle.

2.5. Angular and displacement control

While the XRI is continuously scanning at a constant speed, the respective count rates $C_{1,2}$ reveal the moiré fringes at a constant frequency. If we roughly assume that the effective
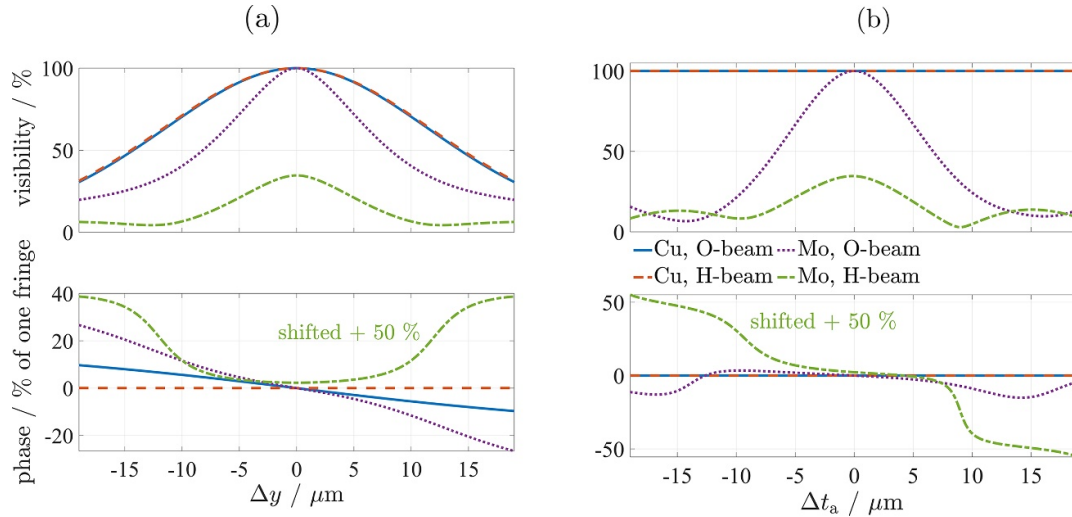
Figure 6. Dependence of fringe visibility and phase of an LLL XRI with 0.4 mm lamellae on defocus (a), i.e. deviation Δy from the optimal mirror-analyzer distance, and the thickness variation of the analyzer lamella Δt_a (b) for O- and H-beam (cf. figure 3(a)) of Cu- and Mo-K$_\alpha$ radiation, respectively, calculated by dynamical x-ray diffraction theory [8, 38, 39]. The phase plots of the Mo-K$_\alpha$ H-beams have been shifted by the denoted amount to improve the readability.

height difference between the upper and lower detector positions is $s \approx 5$ mm, and we would measure at these positions the respective displacements l_1 and l_2 which may include the sought rotation in ρ, then without worrying about arbitrary signs we have

$$|\rho| \approx \frac{|l_2 - l_1|}{s}. \tag{3}$$

For example, the difference $|l_2 - l_1| = d_{220} \approx 192$ pm, i.e. an apparent shift by rotation of one lattice plane between upper and lower channel, corresponds to $|\rho| \approx 40$ nrad. However, the full control interval is only approx. ± 10 nrad corresponding to $\pm d_{220}/4$. Therefore, a proper control must avoid overshoots that could lead to the next order. However, this would strongly reduce the fringe visibility, which is also monitored, and could therefore easily be recognized. In principle, the fringe visibility is maximal when the observed interference is in phase everywhere. This can only be achieved exactly if ρ is zero. To obtain ρ from $C_{1,2}$ we first calculate the complex array

$$Q = [\mathrm{SFT}(C_1)]^* \times \mathrm{SFT}(C_2) \tag{4}$$

where SFT is the scaled Fourier transform described in the appendix of reference [41], and the asterisk denotes the complex conjugate. Let $|q|$ be the first maximum of $|Q|$ after the zero channel of the array. Then, one obtains

$$\rho = \frac{\mathrm{atan2}[\mathrm{Im}(q), \mathrm{Re}(q)]d_{220}}{4\pi s}, \tag{5}$$

where atan2 is the enhanced arcus tangent function which maps unambiguously to the $(-\pi, \pi)$ interval, while Im and Re denote the imaginary and real part respectively.

The measurement data—i.e. the count rates of the four channels and the optical phase ϕ—is taken synchronously on the FPGA board that runs at a clock speed of 120 MHz and needs 2048 samples for each returned phase value. Hence, the measurement data is sampled at a rate of

120 MHz/2048 = 58.593 75 kHz. The sampled data, i.e. each measurement point (MP), consists of a phase value, two COXI counts, and two angle counts. A servo control loop described below provides a constant scanning speed where every 1.024 s 120 moiré fringes are taken. The time-dependence of the data is not explicitly needed anymore and the count rates can directly be related to the optical phase. By this, it is now possible to reorder the count signals: the count rates are re-sampled on an evenly-spaced phase grid—i.e. they are distributed linearly and averaged on that grid according to their corresponding phase value. In figure 7, the frequency spectra of the x-ray translation signal and the optical phase are plotted. When the stage holds its position by using the servo control loop described below, the noise sources are found in the x-ray signal and also in the optical phase. Then, during scan, the noise mixes with the x-ray fringe-frequency of 117.187 5 Hz ($\simeq 23$ nm s^{-1}). By reordering the x-ray counts, one can cancel the mechanical noise almost completely. Typically, reordering increases the contrast from 40–50% to approx. 90%. Nevertheless, we still preserve all the unsorted raw data by saving it to a binary file for later evaluation.

During the scan, three control loops, one for each of the three quantities ρ, θ, and l, are running. A servo loop to control l runs at a frequency of 390.625 Hz and uses the optical phase as input variable. It cancels nonlinearities in the piezo-electric expansion and causes a linear translation and a stable XRI fringe frequency within 0.1 Hz.

The ρ- and θ-loops are both obtained from 6000 MP each. Thus, their control loops run at approx. 9.77 Hz. For the θ-loop, the relatively low photon count rate of approx. 3300 s^{-1} per angle-output channel prohibits a faster control. Although the mean photon count rate of 20 000 s^{-1} per COXI channel is significantly higher, the ρ-loop needs a certain length of data history and computation time to obtain the SFT for the use of (4,5). Actually, a first-in-first-out (FIFO) array of
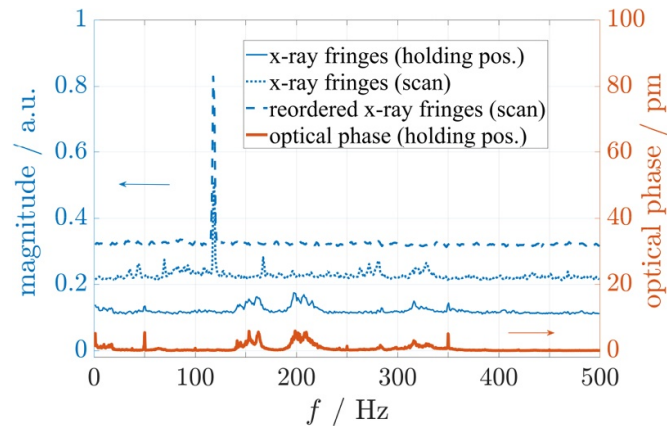
Figure 7. Fourier spectra over frequency *f* in Hz of x-ray fringes (blue curves, assigned to left axis) and of the optical phase in pm (red curve (bottom), assigned to right axis), respectively. The blue curves are shifted vertically by 0.1 a.u. steps to enhance readability. The same noise sources are present in the x-ray signal and optical phase (solid curves). During the scan their frequencies are mixed with the main fringe frequency of 117.1875 Hz (dotted curve). By reordering of the x-ray signal according to a monotonic optical phase the noise can be cancelled (dashed curve). The colors only appear in the online version.

60 000 MP is updated at approx. 9.77 Hz by 6000 MP, and the whole FIFO array is reordered to 6000 points and then subjected to the SFT procedure. The resolution of the digital-to-analog converter controlling the voltage for all piezoelectric actuators is enhanced virtually from 16 to 25 bit by switching at a frequency of 1 kHz, the least significant bit according to a mean-matched duty-cycle in analogy to the HyperBit[TM] technique [42].

The control of the θ-angle is based on the combined count rate of the left angle-interferometer channels. In figure 8, the expected intensity over θ (cf. [32]), obtained by a plane wave dynamical x-ray diffraction simulation [2–6], is plotted. The gray curve in figure 8(a) represents the intended design—i.e. where all lamellae have a thickness of 0.40 mm. The black curve shows the simulation for the achieved thicknesses. While the lamellae of the analyzer crystal have been etched to 0.37 mm, the ones of the splitter/mirror crystal have been etched only to the 0.45 mm thickness. This has shifted the 'bubble', i.e. the highly oscillatory region of angular fringes, away from the center and reduced the oscillation amplitudes. The angle resolution can be seen in figure 8(b). With a realistic deviation within $\pm$ 10% of the signal at the slope, it should be possible to control θ within $\pm$ 0.5 nrad.

2.6. Experiment periphery

Here, for the sake of completeness, we outline the periphery of the experiment. The vacuum chamber rests on a granite platform which is piezoelectrically stabilized by an active vibration isolation system and additionally passively damped by intermediate layers of a visco-elastic material[5] which also prevents the transmission of higher-frequency noise caused by the stabilization system itself. Everything is mounted on a steel framework filled with sand. The so-constructed table is enclosed by a cabin providing acoustic and thermal isolation. The x-ray tube and monochromator are placed outside this cabin and mounted on a hexapod platform to adjust the direction of the x-ray beam towards the experiment. A brass tube ensures radiation safety. Everything else, including the operating personnel, is in a different room.

2.7. Data evaluation, temperature drift and Abbe error

The evaluation of the data of a translation measurement—i.e. phase values and count rates for both channels of the COXI—is done offline for a series of at least 40 or more scans and can be broken down into the following steps for each count channel and scan:

(a) running-average smoothing of the phase to remove high-frequency noise outside mechanical response and hence not useful for reordering;

(b) reordering respective optical-phase count-rate pairs into a monotonic phase array of reduced length while maintaining at least 10 phase values per lattice period;

(c) application of the 4-term Blackman-Harris window to the count channels to reduce spectral leakage [43];

(d) narrow-band discrete Fourier transform (DFT by summation) into the tentative target interval [5.2, 5.215] nm^{-1} with reasonable resolution;

(e) search for the maximum in the DFT result.

In order to compensate the temperature drift between the scans, we can make use of the fact that we do back-and-forth scans. Provided that the drift is comparably slow, while presently a scan of 4 µm takes about 3 min, we can define local averages for each scan in a symmetrical way by weighting the neighbor results with 0.25 and the local result with 0.5.

Typically, the results of the upper and the lower COXI channel do not differ significantly. We use the average of both channels as the result of a single scan. Nevertheless, we can always check for different results. If a significant Abbe error

---

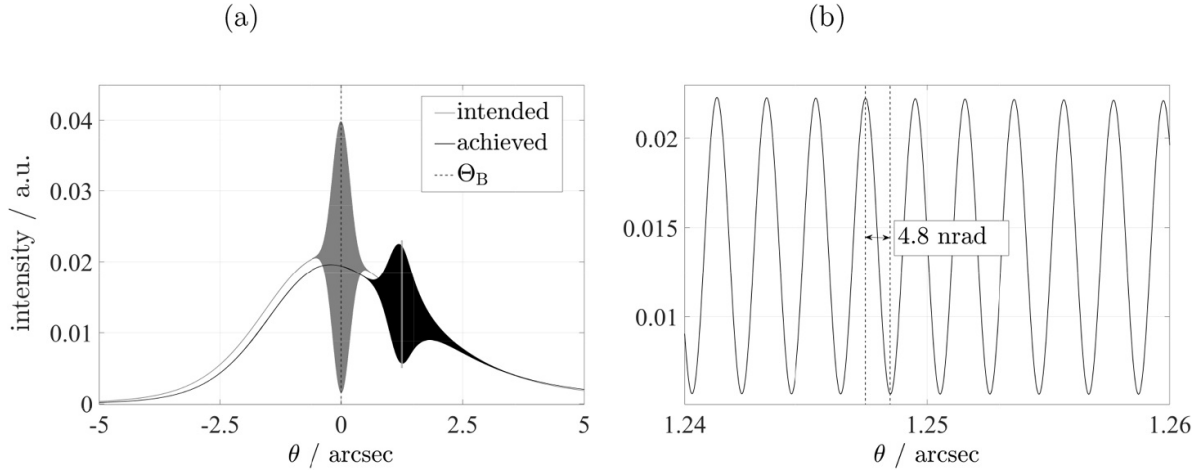[5] Sorbothane, Incorporated, 2144 State Route 59, Kent, OH 44 240, USA (https://www.sorbothane.com).

(a)   (b)

Figure 8. Simulated intensity over angle θ of the left output beam of the x-ray angle-interferometer in figure 3(a). (a) The dashed vertical line indicates the orientation at Bragg angle Θ_B. The gray curve shows the simulated intensity for the intended design, while the black curve does the same for the actually achieved arrangement. The vertical gray line at the center of the black 'bubble' indicates the region of plot (b). The slope over 4.8 nrad can be used to control θ at nanoradian level.

in ρ would be present, then depending on the z-coordinate of the rotation center, it would always affect both channels differently but maintain the same difference owing to $s \approx 5$ mm. For example, if the rotation center is located in the middle, it will affect both channels with a lever arm of approx. $\pm\,2.5$ mm. Therefore, if no significant difference is measured, no significant Abbe error in ρ is present. Additionally, we evaluate the reordered counts of both channels via (4) and (5) to obtain the actual ρ-angles of a scan. This offline evaluation is done almost identical to the online evaluation during the measurement, except that only 6000 MP at a time are reordered to 600 points and then subjected to (4) and (5).

The counts of the angle XRI can be used to check the relevance of the Abbe error in θ. In order to obtain the θ-angles, we assume that the average count rate $\bar{C}$ of a single channel can safely be related to the zero-crossing of the sinusoidal oscillation of the theoretical curve shown in figure 8(b). From this relation, we can infer the extremal count rates $C_{\mathrm{min,max}}$ and map an actual count rate, C, into the interval $[-1, 1]$:

$$\eta(C) = 2\frac{C - \bar{C}}{C_{\mathrm{max}} - C_{\mathrm{min}}}. \qquad (6)$$

From η, we can obtain θ by using the theoretical width of the slope region (cf. figure 8(b)):

$$\theta(\eta) = \frac{\sin^{-1}(\eta)}{\pi} \times 4.8 \text{ nrad}. \qquad (7)$$

This is done for both channels separately, and the average of both channels is used.

Here we add some more details about how to deal with Abbe errors in practice. We refer to the same geometry as in our setup. In principle, the relevant coordinates of the laser beam on the moving mirror in y and z should be chosen as close as possible to the respective coordinates of the rotation centers of ρ and θ to minimize the residual lever arms that contribute to the Abbe error. It is possible and the usual good practice, to

vary the laser beam position and to introduce dedicated known rotations during a scan to obtain the lever arms from the experiment by fit procedures. Remaining Abbe offsets can then be either minimized or considered by respective corrections and uncertainties. It is worth noting that a similar (but less tedious) method is used for the residual angle between beam and mirror normal to obtain the cosine error.

3. Results

In figure 9, a typical DFT of both channels of the COXI is plotted. The central peak is at the fringe frequency of the sought lattice parameter d_{220} of ^{28}Si. The side-lobes appear at $\pm 2/\lambda_m$ from this peak, where $\lambda_m = 532.289\,932\,789$ nm is the wavelength of the measurement beam.

A histogram of the uncorrected lattice parameter d_{220} of ^{28}Si obtained from 100 measurement scans is plotted in figure 10. The distribution follows a normal (Gaussian) probability density function (PDF). We obtain a mean value of $\bar{d}_{220} = 192.014\,790(14)$ pm. The temperature of the measurement setup has been $20.3(4)\,^{\circ}$C. The uncertainty of the temperature is caused by provisional measurement sensors placed outside the vacuum chamber but still in an environment which is stable to a few mK.

In order to check the dependence of the standard deviation σ from the scan length Δl, we evaluate 40 measurement scans and plot the obtained lattice parameter values in figure 11 for different scan lengths. While the actual Δl of that measurement run was 4 µm, we artificially cut out shorter intervals symmetrically around the center of the scans. Figure 12 shows in the double logarithmic scale how $\sigma/192$ pm extrapolates to longer Δl. For comparison we also plotted the results of a Monte Carlo simulation (MCS) involving a Poisson random number generator which is modulated by a sinus function. It mimics the actual data as closely as possible by using the same resolution of 384 fm / MP, 0.34 photon counts / MP, and a contrast of 0.9.
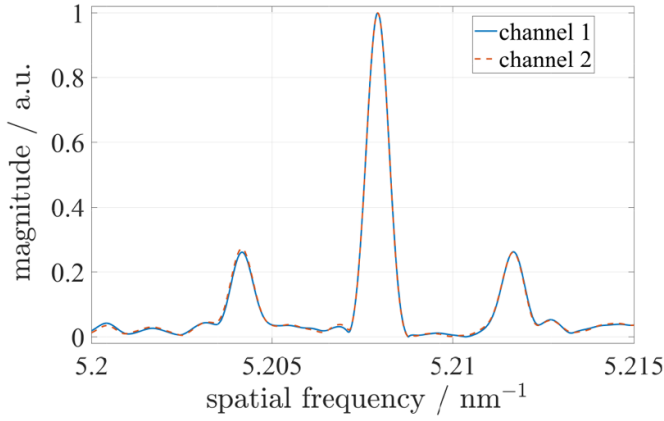
Figure 9. DFT of reordered count signals of the COXI channels over the spatial frequency of respective optical phase. The central peak is at the fringe frequency of the sought lattice parameter d_{220} of ^{28}Si.
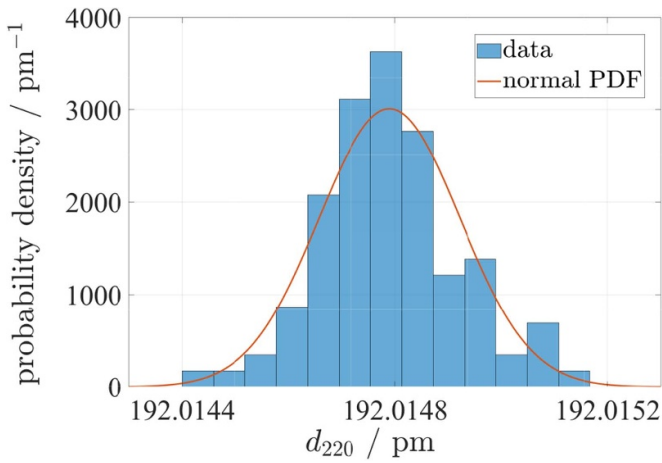

Figure 12. Extrapolation and Monte Carlo simulation (MCS) of the relative standard deviation $\sigma/192$ pm corresponding to figure 11 over the scan length in the double logarithmic scale. The MCS uses a Poisson random number generator (RNG) which is modulated by a sinus function. The fits are linear on the double logarithmic scale.

As an example of a typical single scan over 4 μm, the respective angular distributions, reconstructed from the corresponding count signals, are plotted in figure 13. Each of the 1670 points comprises 6000 count values per channel. Hence, we use the same time resolution as is used for the control loops. Both distributions follow a normal PDF. For θ, we obtain $\sigma = 0.10$ nrad with the mean value $\bar{\theta} = 10$ frad. For ρ, we get $\sigma = 0.27$ nrad with the mean value $\bar{\rho} = 0.03$ nrad.

Figure 10. Histogram of the uncorrected lattice parameter d_{220} obtained from 100 COXI-measurement scans. The red curve shows the respective normal probability density function (PDF). The colors only appear in the online version.
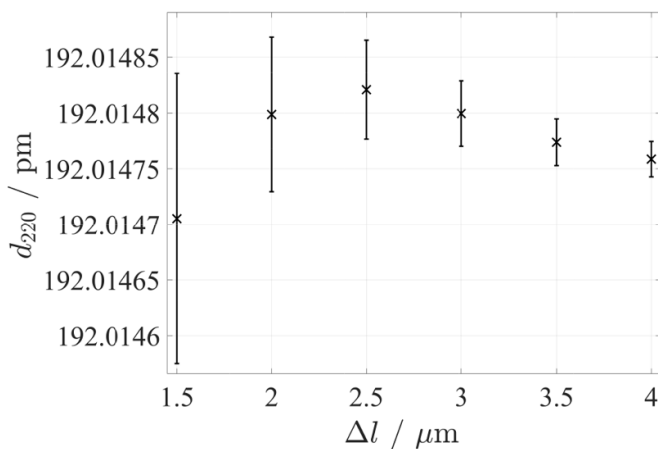
4. Discussion

The DFT shown in figure 9 reveals two side lobes at $\pm 2/\lambda_{\mathrm{m}}$ from the main peak. This likely indicates the presence of residual periodic non-linearities in the optical interferometer phase [36], which enters the XRI phase by the reordering process.

As mentioned before, the given value of the lattice parameter is uncorrected. It can still be affected by the cosine error, which has yet to be determined by measurements under different dedicated incidence angles of the laser beams onto the side mirrors of the COXI. This will be conducted when the setup is capable of reaching the targeted accuracy. Also, misalignment and shearing between measurement and reference beams should be measured and considered as well as possibly reduced by proper adjustment.

State-of-the-art temperature measurement equipment has not been implemented so far, because the focus lied on the demonstration of the new measurement concept. Thus, the uncertainty of the temperature T is not yet in the targeted range of $u(T) \lesssim 3$ mK, which can be expected by comparison with similar setups after proper implementation of the necessary devices, which is of course on our agenda. Currently, we can estimate it to $u(T) \approx 0.4$ K. It is worth noting that for the XRCD method the absolute temperature is not as important as the temperature difference between the volume measurement and the lattice parameter measurement. Therefore, it is unrewarding to state the uncertainty for the absolute temperature, while it

Figure 11. Uncorrected values of the lattice parameter d_{220} of ^{28}Si obtained by 40 COXI-measurement scans evaluated for different scan lengths. The error bars represent the respective standard deviation of the mean.
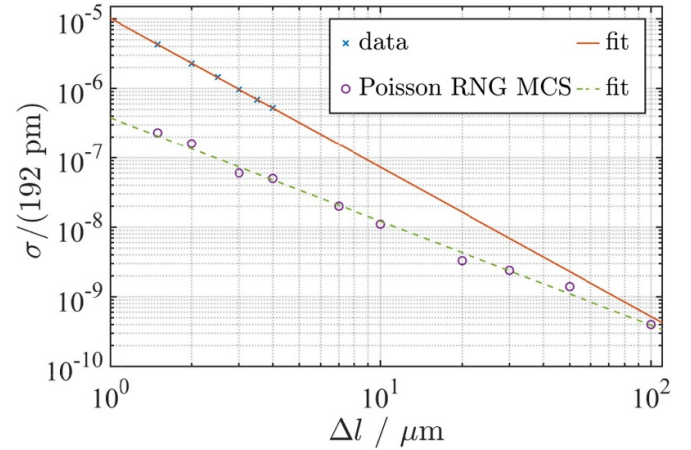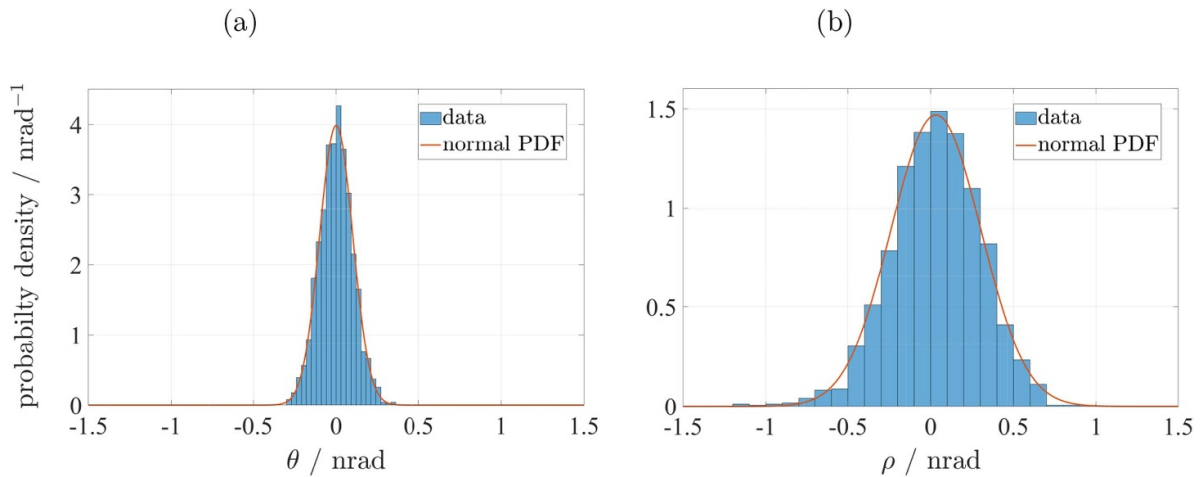
(a) (b)

Figure 13. Histograms of angles θ (a) and ρ (b) are reconstructed from the count signals taken during a single measurement scan. The red curves show the respective normal PDF. The colors only appear in the online version.

is the uncertainty of the difference, which is most important. By temperature comparisons this difference must be checked and its uncertainty kept below 1 mK. In our case, to check the INRIM measurement, we must ensure that the temperature of our lattice parameter measurement is differing by less than 1 mK from the respective temperature of the INRIM measurement.

The extrapolation of the relative standard deviation over the scan length suggests that the targeted relative statistical reproducibility of 3×10^{-9} is principally reachable with 100 measurement scans when the scan length is expanded to $\gtrsim 20$ µm (cf. figure 12). Of course, such an extrapolation is potentially imprecise, and it should not be possible to cross the line given by the MCS. Nevertheless, the extrapolation and simulation have in common that σ reduces linearly on a double logarithmic scale—i.e. to a power in the range between –2.1 and –1.5 with the scan length. The offset of the experiment from the MCS cannot be explained by systematic angle deviations common to all of the 40 scans. The relevant angles are controlled and fluctuate randomly around a well defined almost zero mean. The offset is likely caused by random instabilities of the control loops and other influences.

To summarize, we are confident that our targeted scan length of 100 µm is sufficient to make sure that σ will no longer be a limiting factor, as most of the other uncertainties, especially relating to temperature, will prevail. We have shown how the angles relevant to the Abbe error can be obtained from the measured data and could successfully demonstrate the other main features of this new kind of COXI.

5. Outlook

Next, a translation table with an unloaded resonance frequency of 350 Hz and an open-loop travel range of 600 µm will be inserted to extend the possible scan length. In order to keep the measurement times short, we intend to increase the scanning speed by a factor for 10. This will shift the x-ray fringe-frequency to 1.2 kHz, which is still sufficient to provide

enough photons per MP and does not require other major changes to the setup.

6. Conclusion

We demonstrated the feasibility of a new COXI design based on the fusion of two skew-symmetric XRI in triple and quadruple Laue geometry for displacement and angle, respectively. The presented setup employs single-photon interference to enable continuous scanning, while full control of the relevant angles, θ and ρ, can be ensured at the sub-nanoradian level. This minimizes the Abbe error. Synchronous detection of the phase of the optical interferometer and the count rates of the XRI channels enables direct correlation between the optical phase and the count rates. Reordering the latter over a monotonic optical phase can effectively cancel the mechanically induced noise that is imprinted in the optical and in the XRI phase.

With the currently available scan length of $\Delta l = 4$ µm, we showed that continuous scanning can reduce the scan-length requirement of the decadic step method by more than one order of magnitude. A future update of the setup will enable Δl of up to 600 µm, while a Δl of 100 µm is more than sufficient to achieve the targeted relative statistical reproducibility of the ^{28}Si d_{220} lattice parameter of 3×10^{-9}.

ORCID iD

B Andreas https://orcid.org/0000-0002-0383-6589

References

[1] Bonse U and Hart M 1965 An x-ray interferometer *Appl. Phys. Lett.* **6** 155–6

[2] Huang X R and Dudley M 2003 A universal computation method for two-beam dynamical x-ray diffraction *Acta Cryst.* **A59** 163–7

[3] von Laue M 1960 *Röntgenstrahl-Interferenzen* (Frankfurt am Main: Akademische Verlagsgesellschaft)

[4] Authier A 2001 *Dynamical Theory of X-Ray Diffraction* (New York: Oxford University Press)

[5] Lugovskaya O M and Stepanov S A 1991 Calculation of the polarizabilities of crystals for diffraction of x-rays of the continuous spectrum at wavelengths of 0.1–10 Å *Sov. Phys. Crystallogr.* **36** 478–81

[6] Stepanov S A 1997 X0h on the Web!!! (https://x-server.gmca.aps.anl.gov/x0h.html) (Accessed: 13 March 2017)

[7] Borrmann G 1950 Die Absorption von Röntgenstrahlen im Fall der Interferenz *Z. Physik* **127** 297–323

[8] Bonse U and te Kaat E 1971 The defocussed x-ray interferometer *Z. Physik* **243** 14–45

[9] Lang A R and Miuscov V F 1965 Å-scale displacements revealed by x-ray moiré topographs *Appl. Phys. Lett.* **7** 214–16

[10] Hart M 1968 An ångström ruler *J. Phys. D* **1** 1405–8

[11] Basile G *et al* 2000 Combined optical and X-ray interferometry for high-precision dimensional metrology *Proc. R. Soc. Lond.* A **456** 701–29

[12] Bonse U and te Kaat E 1968 A two-crystal x-ray interferometer *Z. Physik* **214** 16–21

[13] Deslattes R D 1969 Optical and x-ray interferometry of a silicon lattice spacing *Appl. Phys. Lett.* **15** 386–8

[14] Bonse U, te Kaat E and Spieker P 1971 *Precision Lattice Parameter Measurement by X-Ray Interferometry* (*NBS Special Publications* vol 343) eds D N Langenberg and B N Taylor (Washington: DC: U.S. Government Printing Office)

[15] Becker P and Bonse U 1974 The skew-symmetric two-crystal x-ray interferometer *J. Appl. Cryst.* **7** 593–8

[16] Becker P *et al* 1981 Absolute measurement of the (220) lattice plane spacing in a silicon crystal *Phys. Rev. Lett.* **46** 1540–3

[17] Becker P, Seyfried P and Siegert H 1982 The lattice parameter of highly pure silicon single crystals *Z. Phys.* B **48** 17–21

[18] Becker P 2003 Tracing the definition of the kilogram to the Avogadro constant using a silicon single crystal *Metrologia* **40** 366–75

[19] Cavagnero G, Fujimoto H, Mana G, Massa E, Nakayama K and Zosi G 2004 Measurement repititions of the Si(220) lattice spacing *Metrologia* **41** 56–64

[20] Massa E, Mana G, Kuetgens U and Ferroglio L 2011 Measurement of the 220 lattice-plane spacing of a ^{28}Si x-ray interferometer *Metrologia* **48** S37–S43

[21] Massa E, Mana G, Sasso C P and Palmisano C 2015 A more accurate measurement of the ^{28}Si lattice parameter *J. Phys. Chem. Ref. Data* **44** 031208

[22] Andreas B *et al* 2011 Determination of the Avogadro constant by counting the atoms in a ^{28}Si crystal *Phys. Rev. Lett* **106** 030801

[23] Andreas B *et al* 2011 Counting the atoms in a ^{28}Si crystal for a new kilogram definition *Metrologia* **48** S1–S13

[24] Azuma Y *et al* 2015 Improved measurement results for the Avogadro constant using a ^{28}Si-enriched crystal *Metrologia* **52** 360–75

[25] Bartl G *et al* 2017 A new ^{28}Si single crystal: counting the atoms for the new kilogram definition *Metrologia* **54** 693–715

[26] Kuramoto N, Mizushima S, Zhang L, Fujita K, Azuma Y, Kurokawa A, Okubo S, Inaba H and Fuji K 2017 Determination of the Avogadro constant by the XRCD method using a ^{28}Si-enriched sphere *Metrologia* **54** 716–29

[27] Wood B and Bettin H 2019 The Planck constant for the definition and realization of the kilogramm *Ann. Phys.* **531** 1800308

[28] Ferroglio L, Mana G and Massa E 2008 Si lattice parameter measurements by centimeter X-ray interferometry *Opt. Express* **16** 16877–88

[29] Rode G and Jex H 1999 Quantum beats observed in time resolved X-ray interference experiments *Phys. Lett.* A **251** 236–40

[30] Kuetgens U, Andreas B, Friedrich K, Weichert C, Köchert P and Flügge J 2018 Measurement of the silicon lattice parameter by scanning single photon x-ray interferometry *Proc. CPEM 2018: Conf. on Precision Electromagnetic Measurements (8–13 July Paris, FR)* (New York: IEEE) p 689

[31] Köning R, Flügge J and Bosse H 2007 A method for the in situ determination of Abbe errors and their correction *Meas. Sci. Technol.* **18** 476–81

[32] Windisch D and Becker P 1992 Angular measurements with x-ray interferometry *J. Appl. Cryst.* **25** 377–83

[33] Dettmer A, Jäger V and Kuetgens U 1995 Machining of a monolithic silicon x-ray interferometer: a challenge for manufacturing *Proc. 8th Int. Precision Engineering Seminar (May 1995 Compiegne, France)* (Amsterdam: Elsevier) 553–6

[34] Schwartz B and Robbins H 1960 Chemical etching of silicon: II. The system HF, HNO_3, H_2O and $HC_2H_3O_2$ *J. Electrochem. Soc.* **107** 108–11

[35] Weichert C, Köchert P, Quabis S and Flügge J 2017 A displacement interferometer for the calibration of the silicon lattice parameter *Proc. 17th Int. Conf. European Society for Precision Engineering and Nanotechnology* (29 May – 2 June 2017 Hannover, DE) (Northampton: twenty10) p 327

[36] Weichert C, Köchert P, Köning R, Flügge J, Andreas B, Kuetgens U and Yacoot A 2012 A heterodyne interferometer with periodic nonlinearities smaller than $\pm$ 10 pm *Meas. Sci. Technol.* **23** 094005

[37] Schnatz H and Mensing F 2001 Iodine- stabilized, frequency-doubled Nd:YAG lasers at $\lambda = 532$ nm: design and performance *Proc. SPIE* **4269** 239–47

[38] Petrascheck D and Folk R 1976 Theory of a symmetric LLL interferometer with arbitrary absorption *Phys. Stat. Sol* A. **36** 147–59

[39] Bonse U and Graeff W 1977 X-ray and neutron interferometry *Topics in Applied Physics* vol 22 (Berlin, Heidelberg: Springer)

[40] Ferroglio L, Mana G and Massa E 2011 The self-weigh deformation of an x-ray interferometer *Metrologia* **48** S50–S54

[41] Nascov V and Logofătu P C 2009 Fast computation algorithm for the Rayleigh-Sommerfeld diffraction formula using a type of scaled convolution *Appl. Opt.* **48** 4310–9

[42] PI 2006 Whitepaper (https://www.pi-usa.us/fileadmin/user_upload/pi_us/files/technotes_whitepapers/HypderBitTechnology_Improves_NanoPositioning_Resolution.PDF.pdf) (Accessed: 31 Jan 2020)

[43] Harris F J 1978 On the use of windows for harmonic analysis with the discrete fourier transform *Proc. IEEE* **66** 51–83